Neon isotopic composition of the mantle constrained by single vesicle analyses

Sandrine Péron [a], Manuel Moreira [a], Aurélia Colin [a], Laurent Arbaret [b,c,d], Benita Putlitz [e], Mark D. Kurz [f]

[a] Institut de Physique du Globe de Paris - Sorbonne Paris Cité, UMR CNRS 7154, Université Paris Diderot. 1 Rue Jussieu, 75005, Paris, France

[b] Université d'Orléans, ISTO, UMR 7327, 45071 Orléans, France

[c] CNRS/INSU, ISTO, UMR 7327, 45071 Orléans, France

[d] BRGM, ISTO, UMR 7327, BP 36009, 45060 Orléans, France

1A rue de la Férolerie, 45071 Orléans Cédex 2

[e] Institute of Earth Sciences, University of Lausanne, Géopolis Building, CH-1015 Lausanne, Switzerland

[f] Marine Chemistry and Geochemistry, MS #25, Clark 421, Woods Hole Oceanographic Institution, Woods Hole, MA 02543, United States

Corresponding author: Sandrine Péron, peron@ipgp.fr

Revision submitted to Earth and Planetary Science Letters on May 27, 2016

The definitive version was published in Earth and Planetary Science Letters 149 (2016), 145-154

http://dx.doi.org/10.1016/j.epsl.2016.05.052

Abstract: The origin of volatiles on Earth is still a matter of debate. Noble gases are an efficient geochemical tool to constrain Earth formation processes due to their inertness. Several studies have focused on the neon isotopic composition of the lower mantle because the $^{20}Ne/^{22}Ne$ ratio is thought to reflect that of Earth's primordial components. Two models to explain the origin of light noble gases on Earth have been proposed: either solar wind implantation onto the Earth's solid precursors or dissolution into the mantle of a primordial atmosphere captured from solar nebula gas. In order to test these two models, we analyzed the noble gas compositions (helium, neon and argon) of two submarine oceanic island basalt glasses from Fernandina volcano (Galápagos archipelago), which have among the most primitive/unradiogenic terrestrial helium and neon isotopic compositions. Several sample pieces are studied both by step-crushing and by laser ablation analyses of single vesicles. Results of step-crushing are consistent with those of laser ablation analyses, but the latter results provide new insights into the origin of atmospheric contamination. The single-vesicle laser-ablation measurements overlap with the step crushing results, but have systematically higher $^{40}Ar/^{36}Ar$, and $^{3}He/^{36}Ar$, suggesting less atmospheric contamination using this method. The single vesicle data therefore suggest that atmospheric contamination is introduced by exposure to the modern atmosphere, after sample collection. $^{3}He/^{4}He$ values are about 23 times the atmospheric ratio (R/Ra) for the two Fernandina (Galápagos) samples, in agreement with previous studies. We obtain $^{20}Ne/^{22}Ne$ and $^{40}Ar/^{36}Ar$ isotopic ratios as high as 12.91 and 9400, respectively, for the mantle source of the Galápagos hotspot. The new data show that step-crushing and laser ablation analyses are complementary methods that should be used together to derive the noble gas ratios in uncontaminated samples. The results of neon compositions are consistent with previous hotspot studies and support the model of solar wind implantation associated with sputtering to explain helium and neon origins on Earth.

Keywords: oceanic island basalts, Galápagos, lower mantle, helium, neon, argon isotopes

I) Introduction

The origin of volatiles on Earth is still a matter of intense research, but is fundamental to understanding Earth and atmosphere formation processes. Noble gases are important tools to address this problem due to their chemical inertness. In particular, neon gives precious information on that question. Neon has three isotopes of masses 20, 21 and 22, which can all be produced by nucleogenic reactions (e.g. $^{18}O(\alpha,n)^{21}Ne$). However, the production rates of isotopes ^{20}Ne and ^{22}Ne are negligible in the terrestrial mantle (Yatsevich and Honda, 1997), so the $^{20}Ne/^{22}Ne$ ratio of the mantle reflects the primitive neon composition. Many studies have put forward that the mantle $^{20}Ne/^{22}Ne$ ratio is higher than 12 and is therefore "solar-like" (Ballentine et al., 2005; Honda et al., 1993; Kurz et al., 2009; Moreira et al., 1998; Mukhopadhyay, 2012; Raquin and Moreira, 2009; Sarda et al., 1988; Trieloff et al., 2000). By comparison, the atmospheric $^{20}Ne/^{22}Ne$ ratio is 9.78 ± 0.03 (Sano et al., 2013) and the solar wind ratio, measured on the Genesis targets, is 13.78 ± 0.03 (1σ) according to Heber et al. (2009) or 14.001 ± 0.042 (1σ) according to Pepin et al. (2012). The solar wind is isotopically fractionated compared to the Sun, which, by calculation, has a $^{20}Ne/^{22}Ne$ ratio of 13.34 using an inefficient Coulomb drag model (Heber et al., 2012).

It is essential to precisely measure the neon composition of the lower mantle. Indeed, the lower mantle must reflect a less degassed reservoir than the upper mantle and still contains primordial noble gas components, in particular primordial helium (^3He) and neon (Allègre et al., 1983; Kaneoka and Takaoka, 1980; Kurz et al., 2009; Valbracht et al., 1997). In contrast, the upper mantle is considered to be more degassed of its primordial noble gases and should be more sensitive to subduction of atmospheric noble gases. Only a few hotspots are well-suited to determine the lower mantle noble gas composition, namely Hawaii, Galápagos and Iceland, because fresh submarine glass samples, erupted at great depths, are required to obtain accurate neon analyses. Submarine glasses are among the best samples for recording the quenched magma (mantle) noble gas composition directly after eruption.

77 Several studies have focused on the lower mantle composition and have led to two opposing models
78 for the origin of noble gases on Earth. Trieloff et al. (2000) found that oceanic island basalts (OIB) from
79 Hawaii and Iceland showed a mean $^{20}Ne/^{22}Ne$ ratio of 12.49 ± 0.06 (1σ), very close to that of the Neon
80 B component observed in gas-rich meteorites and on the lunar soil (Black, 1972). They argued that since
81 there were no extant terrestrial measurements higher than ~ 12.5, Neon B was the likely terrestrial end-
82 member, assumed to be derived from solar wind implantation (Black, 1972). Hence, Trieloff et al. (2000)
83 suggested that planetesimals that accreted to form the Earth had suffered solar wind implantation and
84 were then characterized by the Neon B component. However, Yokochi and Marty (2004) measured a
85 $^{20}Ne/^{22}Ne$ ratio of 13.04 ± 0.2 (1σ) in plume-related rocks from the Kola peninsula (Russia), which led
86 them to propose that this ratio of 13 would represent a lower limit for the lower mantle neon
87 composition and that terrestrial neon would come from the dissolution of solar nebula gas into the
88 mantle. The latter scenario, also advocated by Mukhopadhyay (2012), implies that the solar nebula gas
89 remained in the accretion disk long enough to permit the capture of a primordial atmosphere, an
90 important temporal constraint for the early Earth. Raquin and Moreira (2009) developed a model that
91 would explain implanted $^{20}Ne/^{22}Ne$ ratio, starting from solar wind values of ~ 13.8, by isotopic
92 fractionation during implantation and erosion on the grain surfaces. In this model, lighter isotopes are
93 preferentially lost from accreting and eroding grains due to their lower energy, shorter implantation
94 depth, and preferential loss by erosion. Raquin and Moreira (2009) were able to derive a steady state
95 $^{20}Ne/^{22}Ne$ of ~ 12.5 for accreting particles, using reasonable values of exposure time and erosion rates.
96 However, the timing and geometries (particle sizes) of accretion are poorly known, so higher steady
97 state values (such as 12.7) are possible (Moreira, 2013). In all accretion models, whether gases are
98 introduced by implantation on solid grains or by equilibration with nebular gas, the neon isotopic
99 composition of the Earth's interior is one of very few constraints.
100 One of the major problems in noble gas geochemistry is the ubiquity of an air-like noble gas
101 component in mantle-derived samples. Step-crushing experiments always consist of mixing between an
102 air-like component and a mantle component as shown by many studies (e.g., Trieloff et al. (2000) and

Yokochi and Marty (2004)). Ballentine and Barfod (2000) suggested that this air-like component is due to atmospheric contamination such that air fills the many cracks and microfractures within samples once they are brought to the surface. Conversely, Sarda (2004) suggested that this air-like component could correspond to atmospheric noble gas recycling into the mantle and that the larger vesicles would carry this recycled component. Several studies (e.g., Holland and Ballentine (2006), Parai and Mukhopadhyay (2015) and Tucker et al. (2012)) have now suggested that both processes (shallow level contamination and recycling through subduction) may occur for heavy noble gases (Ar, Kr, Xe) whereas light noble gases (He, Ne) would not be significantly recycled into the mantle (Holland and Ballentine, 2006). Burnard et al. (1997) and Burnard (1999) introduced laser ablation analyses of single vesicles and never found vesicles filled with air. Raquin et al. (2008) showed that laser ablation analyses can (partly) remove this shallow level atmospheric contaminant and therefore is a promising method to determine the true mantle isotopic composition.

In this study, we focus on OIB samples from one of the most primitive hotspots for helium, the Galápagos hotspot (Kurz et al., 2009; Kurz and Geist, 1999) in order to determine their helium, neon and argon compositions and to constrain which of the two models for the origin of noble gases on Earth is best supported by the data. In addition to step-crushing experiments, we conduct laser ablation analyses on single vesicles. Since OIB samples are not very vesicular, pieces of samples for laser ablation are characterized with X-ray microtomography, a powerful and non-destructive technique, which allows precise location of vesicles in samples.

II) Samples and methods

2.1 Sample selection

Two samples from Fernandina volcano (Galápagos hotspot) collected during the AHA-NEMO2 cruise are studied, samples AHA-NEMO2-D22A and AHA-NEMO2-D22B from a single dredge on the

submarine western flank. Details about sample location can be found in Geist et al. (2006); helium and neon data for D22B and a number of other Fernandina samples can be found in Kurz et al. (2009).

These two samples were selected for their thick basaltic glassy pillow lava margins, which allowed the use of intact large (centimeter sized) glass chunks for the laser ablation and step crushing measurements. They are assumed to have recorded the quenched magma composition directly after eruption, without having suffered intense post-eruptive processes (such as slow cooling or crystallization). For such a study, it is best to choose samples collected at great water depth so that vesicle internal pressures are high when the magma is quenched (approximately equal to hydrostatic pressure (Colin et al., 2013)), increasing the likelihood of gas-rich vesicles. The two studied samples were dredged between 2210 and 2390 meters deep.

2.2 X-ray microtomography

Before laser ablation analyses, pieces of samples were imaged via X-ray microtomography in order to locate the vesicles. X-ray computed microtomography is a powerful and non-destructive technique, which permits the reconstruction of the 3D volume of geological samples. The analyses were performed at the Institut des Sciences de la Terre at Orléans and at the Institute of Earth Sciences, University of Lausanne.

Sample pieces are first polished so as to make rectangular shapes of 5-8 mm high, 3-5 mm long and 2-5 mm wide. This ensures easy focusing of the laser beam. Details about X-ray microtomography principles and acquisition parameters can be found in Supplementary Information. Using the X-ray microtomography data, the internal 3D volume, and surfaces, of the sample were reconstructed with different softwares (CTvox, ImageJ, etc) in order to locate vesicles. Figure 1a shows one piece of the sample AHA-NEMO2-D22B obtained with Brucker's software CTvox. As explained in Supplementary Information, each slice corresponds to a transverse section of the sample: this is shown in Figure 1b and Figure 1c. In this way, we can identify vesicle positions and measure their diameters and depths before

piercing them with the laser. This preliminary work is of huge importance since these OIB samples are not heavily vesiculated and also allows evaluation whether vesicles are intact or connected to the surface with cracks.

Sample vesicularities were estimated with ImageJ software (details about calculations are explained in Supplementary Information). Estimated vesicularities are low: on the order of 3-4 % for the two Galápagos samples (refer to Table S2 in Supplementary Information). These low vesicularities demonstrate the importance of X-ray microtomography for single vesicle analyses.

2.3 Step-crushing and laser ablation analyses

All pieces of samples were cleaned in successive ethanol and acetone baths before the analyses. If some weathering marks were still detected with the binocular microscope, samples were further cleansed with oxalic acid (1 %).

Pieces of samples for step-crushing analyses were loaded into crushers, which were baked under ultra-high vacuum between 100-150 °C for at least one night before starting the experiments in order to remove atmospheric noble gases adsorbed onto the sample surfaces and the crusher walls. The sample AHA-NEMO2-D22B was analyzed by step-crushing both at IPGP and at Woods Hole Oceanographic Institution (WHOI). The analyses at WHOI were conducted following the same procedure described by Kurz et al. (2009), but involved a much larger sample size and included argon measurements for each step. There is excellent overall agreement between the step crushing results in the two laboratories, as discussed further below.

For laser ablation analyses, pieces of samples were set in a laser cell which was also baked at 100 °C for at least two days. Since vesicles have been located via X-ray microtomography, we could pierce them with the laser. The laser used was an argon fluoride excimer laser of wavelength 193 nm (ATLEX-300i system). The laser was run at a frequency of 100 Hz with energy of 1.2 to 2 mJ per pulse of 3-7 ns. The laser beam reached a maximum depth of about 100-150 μm in 5-6 min with energy of 2

mJ per pulse. To pierce a vesicle, a one to six minutes laser shot was made. The pressure in the laser cell was measured with a MKS Baratron® manometer. If a vesicle was reached, there was a sudden pressure jump of 0.0050-0.0650 Torr depending on vesicle size. If no vesicle was pierced, the laser cell was pumped for one minute. Several cycles of ablation/pumping were needed to reach some vesicles located more than 100-150 μm deep. In order to derive the quantity of CO_2 in the vesicles, the manometer was calibrated with an air standard. We then assumed that the major gas in the vesicles is CO_2 (Moore et al., 1977).

Once gases were released, either by crushing or by laser ablation, they were purified with a Ti-getter (which was first at 1073 K and then at ambient temperature) and a SAES getter before being trapped onto activated charcoal at about 14 K. Noble gases were then analyzed one after the other with the Noblesse multi-collector mass spectrometer (Nu instruments ©). Neon abundances and isotopic ratios have to be corrected *a posteriori* for interferences between ^{20}Ne and HF^+, $^{40}Ar^{++}$ and also between ^{22}Ne and CO_2^{++}. To do that, a scan at mass 20, mainly composed of HF, was made before introducing the neon into the mass spectrometer, and $^{40}Ar^+$ as well as CO_2^+ were also measured during neon cycles. Since the double-to-single charge ratios $^{40}Ar^{++}/^{40}Ar^+$ and CO_2^{++}/CO_2^+ were determined on the Noblesse mass spectrometer during the analyses (0.075 and 0.01 respectively), neon isotopic ratios can be derived.

Blanks are of huge importance, especially for laser ablation analyses because the gas quantity in a single vesicle is relatively small. Blank analyses were performed in the same way as for sample analyses. For example, if the laser shot to reach a vesicle lasted five minutes, we pierced the sample matrix during five minutes and then corrected the vesicle analysis with the corresponding matrix blank. The matrix blank compositions are indicated in Tables S3a and S3b in Supplementary Information. We started laser ablation as soon as blanks of the line (only with the laser cell and without the crushers) were about $2.8x10^{-10}$ cm^3 of ^4He, less than $2.5x10^{-13}$ cm^3 of ^{22}Ne and less than $2.2x10^{-12}$ cm^3 of ^{36}Ar. For step-crushing experiments, typical blanks were about $5.0x10^{-11}$ cm^3 of ^4He, $1.3x10^{-13}$ cm^3 of ^{22}Ne and less than $4.0x10^{-12}$ cm^3 of ^{36}Ar. Once the experiments were started, blanks were measured every day; they remained stable and even tend to decrease.

Two standards are used in the present study: an air standard using a pipette connected to a 1 liter reservoir in which 0.410 cm^3 of air was expanded, and a homemade standard at the IPGP laboratory dedicated to He and Ne analyses in He-Ne poor samples. The latter was obtained by crushing 120 g of the MORB sample MD57 D9 from Indian Ocean, 7.947 g of sample PNDR6 from Pitcairn hotspot and 64.15 g of the MORB sample EW9309 33Dsg from South Atlantic. The standard was calibrated against air and the isotopic ratios are $^3He/^4He$ = 7.73 Ra, $^{20}Ne/^{22}Ne$ = 9.94, $^{21}Ne/^{22}Ne$ = 0.0309. Each pipette of the standard corresponds to $9.63x10^{-8}$ cm^3STP of ^4He and $3.56x10^{-12}$ cm^3STP of ^{22}Ne. This standard was used for He and Ne measurements in vesicles and He analyses in crushing steps, whereas the air standard was used for Ne and Ar isotopic measurements in crushing steps.

III) Results

Noble gas abundances and isotopic compositions for step-crushing and laser ablation analyses are given in Table 1 to 4.

3.1 Helium and radiogenic argon

Helium measurements are presented relative to atmosphere (Table 2 and Table 4), where the sample $^3He/^4He$ isotopic ratio (R) is reported relative to the atmospheric ratio (Ra) of $1.384x10^{-6}$ (Clarke et al., 1976). As shown in Table 4, vesicles of the same sample have homogeneous helium isotopic compositions, and the results of step-crushing (Table 2) are consistent with the laser ablation results for $^3He/^4He$. The sample AHA-NEMO2-D22A has a mean $^3He/^4He$ of 23.4 ± 0.3 Ra (1σ) with step-crushing analyses and a mean of 22.6 ± 0.2 Ra (1σ) with vesicles analyses. The sample AHA-NEMO2-D22B has a mean $^3He/^4He$ between 23.0 ± 0.3 Ra (1 σ) (WHOI) and 23.2 ± 0.4 Ra (1σ) (IPGP) with step-crushing analyses and of 23.0 ± 0.5 Ra (1σ) with laser ablation results. The mean $^3He/^4He$ values are lower for vesicle analyses but are nearly the same within uncertainties as those derived through step-

232 crushing analyses. Such values are close to those found by Kurz et al. (2009) (23.07 ± 0.10 for sample
233 AHA-NEMO2-D22A and 22.45 ± 0.10 for sample AHA-NEMO2-D22B).

234 The $^{4}He/^{40}Ar^{*}$ ratio is a proxy of degassing processes ($^{40}Ar^{*}$ is radiogenic ^{40}Ar and is calculated
235 by subtracting the atmosphere composition to the measured ^{40}Ar). Indeed, ^{4}He and $^{40}Ar^{*}$ are two
236 radiogenic isotopes produced by the decay of ^{235}U, ^{238}U and ^{232}Th for helium and by the decay of ^{40}K
237 for argon, and the (U+Th)/K ratio is relatively homogeneous in the lower mantle (Arevalo et al., 2009).
238 The $^{4}He/^{40}Ar^{*}$ production ratio varies from 2 to 5 (Moreira and Kurz, 2013). Since helium is nine times
239 more soluble in a tholeiitic melt than argon (Jambon et al., 1986), helium and argon would be
240 fractionated if a magma was degassed during its ascent to the surface, leading to a higher $^{4}He/^{40}Ar^{*}$
241 ratio than the production ratio. The two Galápagos samples have $^{4}He/^{40}Ar^{*}$ ratios similar to the
242 production ratio (about 2.9 for step-crushing and laser ablation results indicated in Table 2 and Table 4),
243 so we assume that these two samples represent a nearly non-degassed magma.
244
245 3.2 Neon and argon isotopic ratios
246
247 The neon isotopic compositions of the two Galápagos samples are presented in Figure 2 for the
248 step-crushing and laser ablation analyses. Only vesicles for which the matrix blank contribution is less
249 than 60 % (and in most cases less than 30 %) are considered to be reliable: this includes four vesicles of
250 sample AHA-NEMO2-D22A and the vesicles V5 and V6 of sample AHA-NEMO2-D22B (Table 4).
251 Step-crushing data show mixing between an atmospheric component and a mantle-derived component.
252 The highest $^{20}Ne/^{22}Ne$ ratios measured by step-crushing are 12.68 ± 0.08, 12.72 ± 0.11 and 12.91 ± 0.07
253 (1σ) at IPGP and 12.79 ± 0.05 and 12.85 ± 0.05 (1σ) at WHOI. The data follow the same trend as those
254 of Kurz et al. (2009) but these values are the highest ever determined for the Galápagos hotspot since
255 Kurz et al. (2009) found a $^{20}Ne/^{22}Ne$ ratio as high as 12.57 ± 0.08 (1σ) for Fernandina glasses. These are
256 among the highest terrestrial values, as discussed further below.

The isotopic compositions of single vesicles by laser ablation are very similar to the highest ratios obtained by step-crushing. Two vesicles have a $^{20}Ne/^{22}Ne$ ratio of 12.87 ± 0.2 (1σ). Uncertainties on laser ablation data are larger than for step-crushing data because the blank corrections are more important for vesicles than for the crushing steps, and the quantity of neon introduced into the mass spectrometer is smaller.

As for the $^{21}Ne/^{22}Ne$ ratio, the highest values obtained by step-crushing are between 0.0332 and 0.0341 whereas the $^{21}Ne/^{22}Ne$ ratios of vesicles are 0.0325-0.0330. The extrapolated $^{21}Ne/^{22}Ne$ ratio corresponding to a $^{20}Ne/^{22}Ne$ ratio of 12.9 (the highest value obtained) is about 0.0337.

Figure 3 shows that argon obtained by step-crushing consists of mixing between an air-like component and a mantle component. The highest $^{40}Ar/^{36}Ar$ ratios are between 6605 ± 57 and 6702 ± 76 (1σ) and are associated with the highest $^{20}Ne/^{22}Ne$ ratios (Table 2). Moreover, the laser extracted vesicle data are similar to the highest values obtained by step-crushing even if the $^{40}Ar/^{36}Ar$ ratio presents larger variability, between 6061 ± 653 and 9407 ± 672 (Table 4).

3.3 Elemental ratios

Figure 4 and Figure 5 allow an estimate for the $^{3}He/^{22}Ne$ and $^{3}He/^{36}Ar$ elemental ratios of the Fernandina (Galápagos) source. Step-crushing data on these figures show mixing between an air-like component and a mantle component. The linear correlations observed allow extrapolation of the $^{3}He/^{22}Ne$ and $^{3}He/^{36}Ar$ ratios respectively for the $^{20}Ne/^{22}Ne$ and $^{40}Ar/^{36}Ar$ ratios determined by the analyses (section 3.2). Such a method is consistent only for samples having a $^{4}He/^{40}Ar^{*}$ ratio similar to the production ratio (Moreira and Kurz, 2013) so that elemental fractionation between noble gases (e.g. by degassing) is very unlikely to have occurred.

Considering a $^{20}Ne/^{22}Ne$ ratio of 12.91 (as suggested in Figure 2) for the mantle source of the Galápagos hotspot, the extrapolation gives a $^{3}He/^{22}Ne$ ratio of 1.80 (Figure 4) with the IPGP data and of 1.50 with the WHOI data. This relatively small difference might be due to the use of different glass

chunks (sample heterogeneity). Kurz et al. (2009) determined a lower value of about 1 extrapolated to the maximum $^{20}Ne/^{22}Ne$ ratio of 12.5 (at that time) for Fernandina samples. Trieloff et al. (2000) found a higher ratio of 2.5 and Mukhopadhyay (2012) a similar ratio of about 2 for the Icelandic hotspot. If we consider that the $^{40}Ar/^{36}Ar$ ratio of the Fernandina source is 9400 (as suggested in Figure 3), we can infer that the $^{3}He/^{36}Ar$ ratio of the Fernandina source (and by implication, the lower mantle) is about 0.81 (Figure 5). This is higher than the value of 0.35 found by Raquin and Moreira (2009) for Fernandina (Galápagos) samples and the values of 0.4 and 0.53 for Iceland samples found by Trieloff et al. (2000) and Mukhopadhyay (2012) respectively.

Hence, these results highlight the large contrast between MORB and OIB (Moreira and Kurz, 2013). The MORB source is characterized with a $^{3}He/^{22}Ne$ ratio of at least 5 (Moreira et al., 1998; Tucker and Mukhopadhyay, 2014) and a $^{3}He/^{36}Ar$ ratio of 0.45 (Moreira et al., 1998; Raquin et al., 2008).

IV) Discussion

4.1 The air-like component in oceanic basalts

Step-crushing data are characterized by a mixing between a mantle-like component and an air-like component. The latter has been attributed either to atmospheric contamination (Ballentine and Barfod, 2000) or to atmospheric noble gas recycling into the mantle via subduction (Sarda, 2004) or to both processes for heavy noble gases (Holland and Ballentine, 2006; Parai and Mukhopadhyay, 2015; Tucker et al., 2012). However, none of the pierced vesicles, which span a large range of sizes (diameter ranges from 147 μm to 333 μm, volumes are indicated in Table 3) with high internal pressures, show an atmospheric composition. Several previous authors carried out laser ablation analyses and never found such a component in vesicles, in agreement with our results (Burnard, 1999; Burnard et al., 1997; Colin et al., 2013; Colin et al., 2015; Raquin et al., 2008). The observation that no vesicle, with a high internal

309 pressure, has a pure atmospheric composition argues against the model of Sarda (2004). The latter
310 model suggests that vesicles, in particular the big ones, could have an atmospheric composition because
311 of air recycling through subduction into the mantle. Since the recycled material would be more fertile,
312 this would melt first and generate the first vesicles with an atmospheric composition, which would have
313 more time to grow. Note also that the laser ablation and step-crushing isotopic measurements overlap,
314 but that the laser ablation $^{40}Ar/^{36}Ar$ data are systematically higher as a group, demonstrating less
315 atmospheric contamination (see Figures 3 and 5).

316 Thus samples are likely contaminated by air once they are brought to the surface, as suggested
317 by Ballentine and Barfod (2000). Air would progressively fill cracks and vesicles linked to these cracks.
318 As seen in Figure 1, there are many cracks, including microfractures that are hardly visually noticeable
319 inside the glass, which connect some vesicles to one another or directly to the atmosphere. It is also
320 worth noting that we did not manage to pierce some vesicles (no manometric signal), although located
321 via X-ray microtomography. We suspect that these vesicles must already be open with very tiny cracks
322 and filled with air, so no pressure jump was recorded on the manometer. Indeed if these vesicles are
323 filled with air at atmospheric pressure, the manometer accuracy cannot allow the detection of a pressure
324 jump.

325 We make a simple calculation in order to estimate the signal generated on the Noblesse mass
326 spectrometer by a vesicle and a microfracture of given sizes if they were filled with air. First we
327 consider a large vesicle of 500 μm diameter, which is equivalent to a volume of 0.065 mm^3, and
328 corresponds to the largest size observed in our samples. If the vesicle is filled by air, then there is about
329 $2x10^{-9}$ cm^3 STP of ^{36}Ar in the vesicle since there is 0.934 % argon in the atmosphere and the occurrence
330 of ^{36}Ar represents 0.3364 % (Sano et al., 2013). By comparison, the crushing steps with neon and argon
331 atmospheric ratios have a signal on the order of $6x10^{-10}$ – $5x10^{-9}$ cm^3 STP for ^{36}Ar (refer to Table 1).
332 Making the same calculation for a microfracture of 2500 μm long and 5 μm in diameter (sizes which
333 were observed by microtomography) would yield a signal of $1.2x10^{-12}$ cm^3 STP for ^{36}Ar.

Hence, the atmospheric signature of some crushing steps may be due to one or several vesicles filled with air. Once sample glasses are collected, air may progressively fill the microfractures and the vesicles linked to these cracks. When the sample is placed under ultra-high vacuum for step-crushing analyses, some atmospheric gases at the sample surface are likely to be pumped out. However, the air filling the vesicles may not be completely removed because the cracks are very thin (resulting in very low conductance), unless perhaps the sample is pumped for a very long time.

4.2 Neon and argon compositions of the Galápagos source

Since the results of step-crushing clearly indicate atmospheric contamination, it is difficult to use only these results to constrain the lower mantle composition. However, the vesicle compositions are consistently similar to the highest neon and argon isotopic ratios obtained by step-crushing. The fact that the Ne and Ar data of some vesicles, especially vesicles V1 and V3 of sample D22A (Figure 3), are a bit scattered is likely due to very small gas quantities and to matrix effects related to laser ablation prior to vesicle penetration. Raquin et al. (2008) noticed that the signal of the matrix (which is ablated just before reaching a vesicle) can alter the signal of the vesicles, so the matrix blank correction may not be perfect for these vesicles. This would lower in particular the $^{20}Ne/^{22}Ne$ ratio of these vesicles (Figure 2) since the matrix is imbued with atmospheric gas (Tables S3a and S3b in Supplementary Information). Indeed, it is difficult to apply a perfect matrix blank correction on the vesicle analyses because it is implied to reproduce exactly the same matrix ablation distances/geometry as for the vesicles. This is thus a form of atmospheric contamination, which may affect only the vesicles V1 and V3 of sample D22A. The crushing steps with the highest values must not therefore reflect atmospheric contamination, but instead correspond to mantle gases from several vesicles. Even if laser ablation analyses are associated with larger uncertainties, they are a very useful tool to support the fact that some crushing steps do not reflect any atmospheric contamination, and they allow us then to derive the Galápagos source composition (Figures 2, 4, 5 in particular). Although the single-vesicle data are slightly scattered,

359 they suggest that the upper limit for the Galápagos mantle source $^{20}Ne/^{22}Ne$ ratio is 12.9, which is
360 different from solar wind and Sun's values.

361 Considering the new combination data of step-crushing and laser ablation, the Galápagos source
362 $^{20}Ne/^{22}Ne$ ratio is likely to be 12.9, which is higher than the putative Neon B value of 12.5 suggested by
363 Trieloff et al. (2000). The new Galapagos data are consistent with the actual measurements of Trieloff et
364 al. (2000), Mukhopadhyay (2012) and Colin et al. (2015) who found a maximum $^{20}Ne/^{22}Ne$ ratio of
365 12.85 ± 0.31, 12.88 ± 0.06 and 12.73 ± 0.04 (1 σ), respectively, for Iceland glasses, another hotspot with
366 primitive helium and neon. Such a range is also close, within uncertainty, to the highest value of 13.04 ±
367 0.2 (1σ) obtained for the Kola peninsula (Russia) by Yokochi and Marty (2004).

368 Data can be fitted in Figure 3 with hyperbolas considering mixing between an air-like
369 endmember and a mantle endmember so as to better constrain the Galápagos source argon isotopic
370 composition. At least two hyperbolas can fit the data, defined by different r parameters: r = 3 and r = 14.
371 The r parameter indicates the hyperbola curvature and is defined as the ratio between the air-like
372 endmember $(^{36}Ar/^{22}Ne)_{AIR}$ and the mantle endmember $(^{36}Ar/^{22}Ne)_{MANTLE}$. Thus considering a
373 $^{20}Ne/^{22}Ne$ ratio of 12.9 and a $^{40}Ar/^{36}Ar$ ratio of 9400 for the Galápagos mantle source provides one of
374 the best fits to the data. Hence, such values for the two isotopic ratios may be upper limits for this
375 mantle source. The fact that several hyperbolas (at least two) fit the data in Figure 3 may either be due to
376 matrix effects (Raquin et al., 2008) or to the variation of the atmospheric component (its elemental
377 composition) caused by ultra-high vacuum pumping.

378 We do not present the results for the $^{38}Ar/^{36}Ar$ ratio because of analytical limitations. Blank
379 corrections are quite important due to the very small signals. Further analyses will be required to resolve
380 this analytical challenge so as to determine whether the lower mantle $^{38}Ar/^{36}Ar$ ratio is atmospheric, as
381 suggested by Raquin and Moreira (2009) and Trieloff et al. (2000), or not.

382

383

384

385 4.3 Origin of helium, neon and argon on Earth

386

387 Values of approximately 12.9 for the $^{20}Ne/^{22}Ne$ ratio of the Fernandina mantle source,
388 determined here, are higher than the Neon B values of 12.52 determined by Black (1972), and assumed
389 to be an upper terrestrial mantle limit by Trieloff et al. (2000). However, it is close to the average of
390 12.8 determined for lunar soils by Eberhardt et al. (1972), and 12.73 calculated by Moreira (2013) and
391 Moreira and Charnoz (2016). Raquin and Moreira (2009), Moreira (2013) and Moreira and Charnoz
392 (2016) used a model of solar wind grain implantation coupled to isotope fractionation and loss by
393 sputtering/erosion, in order to determine the steady state value of the implanted solar wind (Neon B).
394 They found a $^{20}Ne/^{22}Ne$ ratio of 12.53 using Heber et al. (2009)'s solar wind value and a $^{20}Ne/^{22}Ne$ ratio
395 of 12.73 with Pepin et al. (2012)'s solar wind value. Their model predicted values similar to the results
396 obtained on gas-rich meteorites and on lunar soils (Black, 1972; Eberhardt et al., 1972), but depends
397 upon sputtering/erosion rates and exposure times. If the exposure time is short, the implanted grains
398 will have $^{20}Ne/^{22}Ne$ close to that of the solar wind, but as exposure time increases, the $^{20}Ne/^{22}Ne$ within
399 the grains decreases due to preferential loss of ^{20}Ne. Over time periods of $\sim 10^5$ years, a steady state is
400 reached, where there is a balance between implantation and erosion and the grain $^{20}Ne/^{22}Ne$ is predicted
401 to approach a single value. Moreira and Charnoz (2016) used a numerical model in order to determine
402 the $^{20}Ne/^{22}Ne$ ratio of a population of grains submitted to solar wind irradiation at the beginning of solar
403 system formation and for different exposure ages. They showed that the mean $^{20}Ne/^{22}Ne$ ratio of a grain
404 population could be higher than the Neon B steady state value and could for example reach 12.9 or even
405 13, if the steady state is not reached (exposure ages lower than a few kyr). It seems likely that all the
406 solar nebula grains may have had different exposure times and some may not have reached the steady
407 state. This may result in a higher $^{20}Ne/^{22}Ne$ ratio than the steady state value in the parent bodies of the
408 Earth. On the contrary, Black (1972) determined a steady state value for Neon B on lunar soils, which
409 have been exposed for hundreds of millions of years to solar wind implantation. Hence, the estimated

410 Galápagos value of 12.9 could easily be explained with such a scenario, and the observed $^{20}Ne/^{22}Ne$
411 terrestrial value places important constraints on the early Earth.

412 The fact that several studies found similar values for OIB (Colin et al., 2015; Mukhopadhyay,
413 2012; Trieloff et al., 2000) may indicate that this might be the upper limit for the lower mantle ratio.
414 This is also consistent with the highest value of Yokochi and Marty (2004), 13.04 ± 0.2 (1 σ) within
415 uncertainties. Ballentine et al. (2005) also put forward that Neon B is likely the major neon component
416 in the upper mantle.

417 Yokochi and Marty (2004) obtained a maximum value of 13.04 ± 0.2 (1 σ) for the $^{20}Ne/^{22}Ne$
418 ratio and suggested that the noble gas composition of the lower mantle is inherited from dissolution of
419 solar nebula gas into a magma ocean. The $^{20}Ne/^{22}Ne$ ratio of the Sun is estimated to be about 13.4
420 (Heber et al., 2012) and so Yokochi and Marty (2004) believed that a proto-atmosphere with a solar
421 composition could have been captured early in Earth's history and would have been partly dissolved into
422 the mantle. In the same way, Mukhopadhyay (2012) considered that the composition of the Iceland
423 mantle source is solar-like. Up to now, no study has yet measured values close to 13.4 neither in
424 MORBs nor in OIBs, which seems to question the solar gas dissolution origin for neon.

425 It can also be argued that the $^{20}Ne/^{22}Ne$ ratio was around 13.4 from the dissolution of a proto-
426 atmosphere into the mantle when the Earth formed and that recycling of atmospheric noble gases into
427 the mantle through subduction over billions of years would have then lowered the $^{20}Ne/^{22}Ne$ ratio to a
428 value of 12.9. It is difficult to explain the terrestrial $^{20}Ne/^{22}Ne$ with this scenario because it requires
429 enough neon dissolution into the Earth's precursors (magma ocean) before the solar nebula was blown.
430 However, the nebula is blown in a few Myr (e.g., Beckwith and Sargent (1996) and Wyatt et al. (2003)).
431 It also implies, in a later stage, atmospheric neon recycling via subduction into the gas-rich lower mantle,
432 i.e. to rapidly transport the dissolved neon into the interior. Finally, if only neon dissolution from solar
433 nebula occurred, then one would expect to detect higher $^{20}Ne/^{22}Ne$ ratios than 12.9 in the lower mantle
434 since neon atmospheric recycling into the lower mantle is unlikely (Holland and Ballentine, 2006;
435 Staudacher and Allègre, 1988) or may not have totally erased the solar signature. Marty (2012) has

proposed that the depleted mantle consists of a mixture between a solar-like endmember and a Neon A endmember (this component is found in chondrites) to explain its $^{20}Ne/^{22}Ne$ ratio. This scenario implies recycling of the Neon A component into the upper mantle, since the latter component may have been brought in a later stage (e.g., O'Brien et al. (2014)). However, even if subduction of heavy noble gases may occur (Holland and Ballentine, 2006; Kendrick et al., 2011; Mukhopadhyay, 2012; Parai and Mukhopadhyay, 2015; Parai et al., 2012; Tucker et al., 2012), subduction of light noble gases (helium and neon) into the upper mantle may be very difficult (Holland and Ballentine, 2006; Staudacher and Allègre, 1988).

However, it is important to note that the two models (solar wind implantation and dissolution of solar nebula gas) are not mutually exclusive. It is possible that a part of the terrestrial neon inventory derives from dissolution of solar nebula gas during the Earth's parent body formation. In this case, the Earth neon would correspond to a mixture between solar neon and solar wind implanted neon and only ~30 % of the Earth neon could come from solar nebula gas to account for the OIB $^{20}Ne/^{22}Ne$ ratio, considering a binary mixing between a solar endmember ($^{20}Ne/^{22}Ne$ = 13.4 (Heber et al., 2012)) and a Neon B endmember.

For all these reasons, the Earth (at least the lower mantle) is likely to have mainly acquired its primordial helium and neon from its solid grain precursors, which would have involved solar wind implantation associated with sputtering. The lower mantle neon isotopic composition would then reflect solar wind neon irradiation, which may not be at steady state, explaining the slightly higher $^{20}Ne/^{22}Ne$. This scenario does not require light noble gas recycling through subduction to account for the lower mantle composition. We note that there are still relatively few hotspot helium, neon and argon measurements, so this conclusion is based on existing data. If the $^{38}Ar/^{36}Ar$ ratio is atmospheric in the mantle as suggested by Trieloff et al. (2000) and Raquin and Moreira (2009), then a more complicated scenario may be put forward for argon origin, unless argon was acquired in the same way as helium and neon.

V) Conclusion

We analyzed two oceanic island basalt glasses from Fernandina volcano (Galápagos) by step-crushing and laser ablation of single vesicles in order to derive their noble gas compositions. This study was carried out with the aim of determining which hypothesis for noble gas origin on Earth is more likely: solar wind implantation associated with sputtering (Raquin and Moreira, 2009; Trieloff et al., 2000) or dissolution of solar nebula gas into the mantle (Yokochi and Marty, 2004).

The data suggest that the mantle source of the Fernandina (Galápagos) samples has a $^{20}Ne/^{22}Ne$ ratio of 12.9 and a $^{40}Ar/^{36}Ar$ ratio of about 9400, consistent with studies on the Iceland hotspot. These two ratios are well constrained with new data from the Fernandina samples. The results of laser ablation analyses provide constraints on the atmospheric component of the step-crushing experiments, and the two methods are hence complementary. The laser ablation single-vesicle measurements have systematically higher $^{40}Ar/^{36}Ar$ than the step crushing experiments, suggesting less atmospheric contamination, making this method promising for obtaining mantle values.

Values close to 12.9 for the $^{20}Ne/^{22}Ne$ ratio of the Galápagos hotspot source are the highest measured so far. They are similar, although slightly higher, to the Neon B composition obtained by Eberhardt et al. (1972) and Raquin and Moreira (2009), Moreira (2013) who respectively found an average of 12.8 and a calculated value of 12.73. The Galápagos source $^{20}Ne/^{22}Ne$ ratio (12.9) is slightly higher than the steady state value of the implanted solar wind coupled to sputtering. This could be explained in two ways. On the one hand, the grains in the accretion disk may not have all reached the steady state, resulting in a mean $^{20}Ne/^{22}Ne$ ratio higher than the steady state, as proposed recently by Moreira and Charnoz (2016). On the other hand, a mixture of dissolved solar neon into planetary embryos having the size of Mars and implanted neon (Neon B) could also produce an isotopic ratio of ~12.9. In this case, only ~30 % of the neon derives from dissolution.

Therefore, even if a solar nebula gas contribution cannot be excluded, the new data are more supportive of the solar wind implantation/sputtering model for explaining the helium and neon origin on Earth.

Acknowledgements

We thank Lukas Baumgartner for his welcome in the Institute of Earth Sciences, University of Lausanne and for his useful remarks on X -ray microtomography. We also thank Déborah Chavrit and Emily Pringle for their constructive comments on the manuscript. M.D.K. gratefully acknowledges the laboratory expertise of Joshua Curtice, and support from NSF OCE in collecting the samples and allowing his participation in this study (OCE-1259218 and OCE-1232985). M.M. acknowledges the financial support from the UnivEarthS Labex program of Sorbonne Paris Cité (ANR-10-LABX-0023 and ANR-11-IDEX-0005-02). Two anonymous reviewers are thanked for their comments, which improved the manuscript.

References

Allègre, C.J., Staudacher, T., Sarda, P., Kurz, M.D., 1983. Constraints on evolution of Earth's mantle from rare gas systematics. Nature 303, 762-766.

Arevalo, R., McDonough, W.F., Luong, M., 2009. The K/U ratio of the silicate Earth: Insights into mantle composition, structure and

thermal evolution. Earth and Planetary Science Letters 279, 361-369.

Ballentine, C., Barfod, D., 2000. The origin of air-like noble gases in MORB and OIB. Earth and Planetary Science Letters 180, 39-48.

Ballentine, C.J., Marty, B., Lollar, B.S., Cassidy, M., 2005. Neon isotopes constrain convection and volatile origin in the Earth's mantle. Nature 433, 33-38.

Beckwith, S.V.W., Sargent, A.I., 1996. Circumstellar disks and the search for neighbouring planetary systems. Nature 383, 139-144.

Black, D.C., 1972. On the origins of trapped helium, neon and argon isotopic variations in meteorites—I. Gas-rich meteorites, lunar soil and breccia Geochimica et Cosmochimica Acta 36, 347-375.

Burnard, P., 1999. The bubble-by-bubble volatile evolution of two mid-ocean ridge basalts. Earth and Planetary Science Letters 174, 199-211.

Burnard, P., Graham, D., Turner, G., 1997. Vesicle-specific noble gas analyses of "popping rock": implications for primordial noble gases in the Earth. Science 276, 568-571.

Clarke, W.B., Jenkins, W.J., Top, Z., 1976. Determination of tritium by mass spectrometric measurement of ^{3}He. The International Journal of Applied Radiation and Isotopes 27, 515-522.

Colin, A., Burnard, P., Marty, B., 2013. Mechanisms of magma degassing at mid-oceanic ridges and the local volatile composition (^{4}He–$^{40}Ar^{*}$–CO_2) of the mantle by laser ablation analysis of individual MORB vesicles. Earth and Planetary Science Letters, 361, 183-194.

Colin, A., Moreira, M., Gautheron, C., Burnard, P., 2015. Constraints on the noble gas composition of the deep mantle by bubble-by-bubble analysis of a volcanic glass sample from Iceland. Chemical Geology 417, 173-183.

Eberhardt, P., Geiss, J., Graf, H., Grögler, N., Mendia, M.D., Mörgeli, M., Schwaller, H., Stettler, A., Krähenbühl, U., Von Gunten, H.R., 1972. Trapped solar wind noble gases in Apollo 12 lunar fines 12001 and Apollo 11 breccia 10046. Proceedings of the third lunar science conference, sup 3 Geochimica et Cosmochimica Acta, The MIT press 2, 1821-1856.

Geist, D., Fornari, D., Kurz , M.D., Harpp, K.S., Soule, S.A., Perfit, M.R., Koleszar, A.M., 2006. Submarine Fernandina: Magmatism at the leading edge of the Galapagos hot spot. Geochemistry, Geophysics, Geosystems 7.

Heber, V.S., Baur, H., Bochsler, P., McKeegan, K.D., Neugebauer, M., Reisenfeld, D.B., Wieler, R., Wiens, R.C., 2012. Isotopic Mass Fractionation of Solar Wind: Evidence from Fast and Slow Solar Wind Collected by the Genesis mission. The Astrophysical Journal 759, 121.

537 Heber, V.S., Wieler, R., Baur, H., Olinger, C., Friedmann, A., Burnett, D.S., 2009. Noble gas
538 composition of the solar wind as collected by the Genesis mission. Geochimica et Cosmochimica Acta
539 73, 7414-7432.
540 Holland, G., Ballentine, C.J., 2006. Seawater subduction controls the heavy noble gas composition of
541 the mantle. Nature 441, 186-191.
542 Honda, M., McDougall, I., Patterson, D.B., Doulgeris, A., Clague, D., 1993. Noble gases in submarine
543 pillow basalt glasses from Loihi and Kilauea, Hawaii: A solar component in the Earth. Geochimica et
544 Cosmochimica Acta 57, 859-874.
545 Jambon, A., Weber, H., Braun, O., 1986. Solubility of He, Ne, Ar, Kr and Xe in a basalt melting in the
546 range 1250-1600°C. Geochemical Implications. Geochimica et Cosmochimica Acta 50, 401-408.
547 Kaneoka, I., Takaoka, N., 1980. Rare gas isotopes in Hawaiian ultramafic nodules and volcanic rocks;
548 constraint on genetic relationships. Science 208, 1366-1368.
549 Kendrick, M.A., Scambelluri, M., Honda, M., Phillips, D., 2011. High abundances of noble gas and
550 chlorine delivered to the mantle by serpentine subduction. Nature geoscience 4.
551 Kurz, M.D., Curtice, J., Fornari, D., Geist, D., Moreira, M., 2009. Primitive neon from the center of the
552 Galápagos hotspot. Earth and Planetary Science Letters 286, 23-34.
553 Kurz, M.D., Geist, D., 1999. Dynamics of the Galapagos hotspot from helium isotope geochemistry.
554 Geochimica et Cosmochimica Acta 63, 4139-4156.
555 Lee, J.-Y., Marti, K., Severinghaus, J.P., Kawamura, K., Yoo, H.-S., Lee, J., Kim, J., 2006. A
556 redetermination of the isotopic abundances of atmospheric Ar Geochimica et Cosmochimica Acta 70,
557 4507-4512.
558 Marty, B., 2012. The origins and concentrations of water, carbon, nitrogen and noble gases on Earth.
559 Earth and Planetary Science Letters 313-314, 56-66.
560 Moore, J.G., Batchelder, J.N., Cunningham, C.G., 1977. CO_2-filled vesicles in mid-ocean basalt. Journal
561 of Volcanology and Geothermal Research 2, 309-327.

562 Moreira, M., 2013. Noble gas constraints on the origin and evolution of Earth's volatiles. Geochemical
563 Perspectives 2, 229-403.
564 Moreira, M., Charnoz, S., 2016. The origin of the neon isotopes in chondrites and on Earth. Earth and
565 Planetary Science Letters 433, 249-256.
566 Moreira, M., Kunz, J., Allègre, C.J., 1998. Rare gas systematics on popping rock : estimates of isotopic
567 and elemental compositions in the upper mantle. Science 279, 1178-1181.
568 Moreira, M.A., Kurz, M.D., 2013. Noble Gases as Tracers of Mantle Processes and Magmatic
569 Degassing, in: Burnard, P. (Ed.), The Noble Gases as Geochemical Tracers. Springer Berlin Heidelberg,
570 pp. 371-391.
571 Mukhopadhyay, S., 2012. Early differentiation and volatile accretion recorded in deep mantle Neon and
572 Xenon. Nature 486, 101-104.
573 O'Brien, D.P., Walsh, K.J., Morbidelli, A., Raymond, S.N., Mandell, A.M., 2014. Water delivery and
574 giant impacts in the 'Grand Tack' scenario. Icarus 239, 74-84.
575 Parai, R., Mukhopadhyay, S., 2015. The evolution of MORB and plume mantle volatile budgets:
576 Constraints from fission Xe isotopes in Southwest Indian Ridge basalts. Geochemistry, Geophysics,
577 Geosystems 16, 719-735.
578 Parai, R., Mukhopadhyay, S., Standish, J.J., 2012. Heterogeneous upper mantle Ne, Ar and Xe isotopic
579 compositions and a possible Dupal noble gas signature recorded in basalts from the Southwest Indian
580 Ridge. Earth and Planetary Science Letters 359-360, 227-239.
581 Pepin, R.O., Schlutter, D.J., Becker, R.H., Reisenfeld, D.B., 2012. Helium, neon, and argon composition
582 of the solar wind as recorded in gold and other Genesis collector materials. Geochimica et
583 Cosmochimica Acta 89, 62-80.
584 Raquin, A., Moreira, M., 2009. Atmospheric $^{38}Ar/^{36}Ar$ in the mantle: Implications for the nature of the
585 terrestrial parent bodies. Earth and Planetary Science Letters 287, 551-558.

586 Raquin, A., Moreira, M., Guillon, F., 2008. He, Ne and Ar systematics in single vesicles: Mantle
587 isotopic ratios and origin of the air component in basaltic glasses. Earth and Planetary Science Letters
588 274, 142-150.
589 Sano, Y., Marty, B., Burnard, P., 2013. Noble Gases in the Atmosphere, in: Burnard, P. (Ed.), The
590 Noble Gases as Geochemical Tracers. Springer Berlin Heidelberg, pp. 17-31.
591 Sarda, P., 2004. Surface noble gas recycling to the terrestrial mantle. Earth and Planetary Science
592 Letters 228, 49-63.
593 Sarda, P., Staudacher, T., Allègre, C.J., 1988. Neon isotopes in submarine basalts. Earth and Planetary
594 Science Letters 91, 73-88.
595 Staudacher, T., Allègre, C.J., 1988. Recycling of oceanic crust and sediments: the noble gas subduction
596 barrier. Earth and Planetary Science Letters 89, 173-183.
597 Trieloff, M., Kunz, J., Clague, D.A., Harrison, D., Allègre, C.J., 2000. The Nature of pristine noble
598 gases in mantle plumes. Science 288, 1036-1038.
599 Tucker, J.M., Mukhopadhyay, S., 2014. Evidence for multiple magma ocean outgassing and
600 atmospheric loss episodes from mantle noble gases. Earth and Planetary Science Letters 393, 254-265.
601 Tucker, J.M., Mukhopadhyay, S., Schilling, J.-G., 2012. The heavy noble gas composition of the
602 depleted MORB mantle (DMM) and its implications for the preservation of heterogeneities in the
603 mantle. Earth and Planetary Science Letters 355-356, 244-254.
604 Valbracht, P.J., Staudacher, T., Malahoff, A., Allègre, C.J., 1997. Noble gas systematics of deep rift
605 zone glasses from Loihi seamount, Hawaii. Earth Planet. Sci. Lett. 150, 399-411.
606 Wyatt, M.C., Dent, W.R.F., Greaves, J.S., 2003. SCUBA observations of dust around Lindroos stars:
607 evidence for a substantial submillimetre disc population. Monthly Notices of the Royal Astronomical
608 Society 342, 876-888.
609 Yatsevich, I., Honda, M., 1997. Production of nucleogenic neon in the Earth from natural radioactive
610 decay. Journal of Geophysical Researchs 102, 10291-10298.

611 Yokochi, R., Marty, B., 2004. A determination of the neon isotopic composition of the deep mantle.
612 Earth and Planetary Science Letters 225, 77-88.

613

614

615

Table 1: Abundances of ^{4}He, ^{22}Ne and ^{36}Ar for the two Galápagos samples analyzed by step-crushing. The new results from WHOI are indicated. For sample AHA-NEMO2-D22A, 9 steps have been carried out and 11 for sample AHA-NEMO2-D22B. For each step, the number of strokes is indicated. Errors are 1 sigma uncertainties. n.a. stands for not analyzed.

Sample	Crush	Weigh g	^{4}He $x10^{-7}$ cm^3/g	^{22}Ne $x10^{-12}$ cm^3/g	^{36}Ar $x10^{-11}$ cm^3/g
AHA-NEMO2-D22A	1x	0.577	3.10 ± 0.09	8.74 ± 0.26	13.6 ± 0.2
AHA-NEMO2-D22A	1x	0.577	4.02 ± 0.12	17.2 ± 0.52	7.61 ± 0.13
AHA-NEMO2-D22A	2x	0.577	6.44 ± 0.19	39.0 ± 1.2	n.a.
AHA-NEMO2-D22A	2x	0.577	2.82 ± 0.08	5.38 ± 0.16	1.51 ± 0.03
AHA-NEMO2-D22A	6x	0.577	3.33 ± 0.10	7.55 ± 0.23	21.2 ± 0.4
AHA-NEMO2-D22A	5x	0.577	2.64 ± 0.08	8.64 ± 0.26	12.7 ± 0.2
AHA-NEMO2-D22A	7x	0.577	2.40 ± 0.07	22.7 ± 0.68	58.5 ± 1.0
AHA-NEMO2-D22A	14x	0.577	1.41 ± 0.04	3.80 ± 0.12	2.67 ± 0.05
AHA-NEMO2-D22A	40x	0.577	1.87 ± 0.06	3.37 ± 0.11	0.95 ± 0.02
AHA-NEMO2-D22B	1x	1.1376	0.40 ± 0.01	1.20 ± 0.04	0.91 ± 0.03
AHA-NEMO2-D22B	5x	1.1376	4.46 ± 0.13	230.9 ± 6.9	482.3 ± 14.5
AHA-NEMO2-D22B	4x	1.1376	1.59 ± 0.05	5.17 ± 0.16	4.89 ± 0.15
AHA-NEMO2-D22B	4x	1.1376	1.63 ± 0.05	3.93 ± 0.12	2.98 ± 0.09
AHA-NEMO2-D22B	5x	1.1376	2.79 ± 0.08	28.2 ± 0.8	43.7 ± 1.31
AHA-NEMO2-D22B	2x	1.1376	1.60 ± 0.05	4.73 ± 0.14	5.22 ± 0.16
AHA-NEMO2-D22B	3x	1.1376	1.49 ± 0.04	5.16 ± 0.16	5.64 ± 0.17
AHA-NEMO2-D22B	6x	1.1376	1.54 ± 0.05	4.47 ± 0.14	6.25 ± 0.19
AHA-NEMO2-D22B	2x	1.1376	1.93 ± 0.06	3.48 ± 0.11	1.03 ± 0.03
AHA-NEMO2-D22B	6x	1.1376	1.28 ± 0.04	3.45 ± 0.11	1.04 ± 0.03
AHA-NEMO2-D22B	6x	1.1376	2.18 ± 0.07	6.21 ± 0.19	2.31 ± 0.07
AHA-NEMO2-D22B WHOI	1x	3.8756	0.38	5.31	9.29
AHA-NEMO2-D22B WHOI	1x	3.8756	0.53	4.07	5.78
AHA-NEMO2-D22B WHOI	1x	3.8756	0.41	1.00	0.46
AHA-NEMO2-D22B WHOI	1x	3.8756	1.31	5.65	5.29
AHA-NEMO2-D22B WHOI	1x	3.8756	0.43	1.01	0.48
AHA-NEMO2-D22B WHOI	1x	3.8756	0.25	1.61	1.47
AHA-NEMO2-D22B WHOI	2x	3.8756	0.60	1.40	0.73
AHA-NEMO2-D22B WHOI	2x	3.8756	0.30	5.00	7.39
AHA-NEMO2-D22B WHOI	3x	3.8756	0.42	15.3	28.8
AHA-NEMO2-D22B WHOI	3x	3.8756	1.38	27.1	47.2
AHA-NEMO2-D22B WHOI	3x	3.8756	0.93	2.82	1.90
AHA-NEMO2-D22B WHOI	3x	3.8756	0.72	27.4	45.7
AHA-NEMO2-D22B WHOI	3x	3.8756	0.35	0.80	0.27
AHA-NEMO2-D22B WHOI	4x	3.8756	1.10	3.85	3.14
AHA-NEMO2-D22B WHOI	4x	3.8756	1.03	8.74	8.61
AHA-NEMO2-D22B WHOI	4x	3.8756	0.50	4.06	5.15
AHA-NEMO2-D22B WHOI	4x	3.8756	0.74	1.87	2.27
AHA-NEMO2-D22B WHOI	4x	3.8756	0.81	1.92	1.11
AHA-NEMO2-D22B WHOI	4x	3.8756	0.57	1.21	0.32
AHA-NEMO2-D22B WHOI	4x	3.8756	0.92	4.21	4.04
AHA-NEMO2-D22B WHOI	4x	3.8756	0.36	2.85	3.87
AHA-NEMO2-D22B WHOI	5x	3.8756	0.34	1.07	0.76
AHA-NEMO2-D22B WHOI	5x	3.8756	0.51	1.41	0.88
AHA-NEMO2-D22B WHOI	6x	3.8756	1.08	2.42	0.64

620 Table 2: Isotopic compositions of the two Galápagos samples analyzed by step-crushing. The new results from
621 WHOI are indicated. Ra is the air $^{3}He/^{4}He$ ratio equals to $1.384x10^{-6}$. $^{40}Ar^{*}$ is radiogenic ^{40}Ar. Errors are 1 sigma
622 uncertainties. n.a. stands for not analyzed and n.d. for not determined. We consider a $^{40}Ar/^{36}Ar$ ratio of 298.6 for
623 the air as obtained by Lee et al. (2006) to determine the $^{40}Ar/^{36}Ar$ and $^{4}He/^{40}Ar^{*}$ ratios.

Sample	Crush	$^{3}He/^{4}He$ (x Ra)	$^{20}Ne/^{22}Ne$	$^{21}Ne/^{22}Ne$	$^{40}Ar/^{36}Ar$	$^{4}He/^{40}Ar^{*}$
D22A	1x	23.57 ± 0.15	11.74 ± 0.06	0.0322 ± 0.0004	1077 ± 2	2.92 ± 0.10
D22A	1x	23.12 ± 0.13	11.18 ± 0.05	0.0312 ± 0.0002	2190 ± 5	2.79 ± 0.10
D22A	2x	23.56 ± 0.14	10.73 ± 0.05	0.0306 ± 0.0002	n.a.	n.a.
D22A	2x	23.45 ± 0.16	12.68 ± 0.08	0.0332 ± 0.0003	6638 ± 56	2.94 ±0.11
D22A	6x	23.67 ± 0.15	12.18 ± 0.07	0.0330 ± 0.0003	824 ± 2	2.99 ±0.10
D22A	5x	23.20 ± 0.13	11.61 ± 0.06	0.0318 ± 0.0004	975 ± 2	3.08 ±0.11
D22A	7x	23.06 ± 0.16	10.42 ± 0.04	0.0300 ± 0.0002	437 ± 1	2.96 ±0.10
D22A	14x	23.67 ± 0.18	11.87 ± 0.10	0.0316 ± 0.0006	2072 ± 10	2.99 ±0.11
D22A	40x	23.08 ± 0.13	12.72 ± 0.11	0.0341 ± 0.0005	6702 ± 76	3.08 ±0.12
D22B	1x	22.72 ± 0.14	11.80 ± 0.10	0.0314 ± 0.0008	1777 ± 24	3.00 ±0.14
D22B	5x	23.44 ± 0.15	9.95 ± 0.04	0.0291 ± 0.0001	335 ± 1	2.52 ±0.16
D22B	4x	22.12 ± 0.14	11.85 ± 0.05	0.0320 ± 0.0004	1544 ± 4	2.62 ±0.11
D22B	4x	23.47 ± 0.15	12.13 ± 0.06	0.0324 ± 0.0004	2147 ± 8	2.96 ±0.13
D22B	5x	23.35 ± 0.14	10.35 ± 0.04	0.0298 ± 0.0001	516 ± 1	2.94 ±0.13
D22B	2x	23.40 ± 0.15	11.82 ± 0.05	0.0319 ± 0.0003	1332 ± 3	2.96 ±0.13
D22B	3x	23.42 ± 0.15	11.41 ± 0.05	0.0314 ± 0.0003	1184 ± 3	2.98 ±0.13
D22B	6x	23.51 ± 0.15	11.78 ± 0.05	0.0322 ± 0.0003	1155 ± 3	2.87 ±0.12
D22B	2x	22.99 ± 0.12	12.91 ± 0.07	0.0336 ± 0.0003	6605 ± 57	2.96 ±0.13
D22B	6x	22.85 ± 0.13	12.02 ± 0.06	0.0328 ± 0.0003	4541 ± 32	2.89 ±0.13
D22B	6x	23.48 ± 0.14	11.92 ± 0.06	0.0323 ± 0.0003	3517 ± 13	2.92 ±0.13
D22B WHOI	1x	23.33 ± 0.57	10.24 ± 0.04	0.0295 ± 0.0003	436 ± 6	2.87
D22B WHOI	1x	23.73 ± 0.58	10.70 ± 0.04	0.0302 ± 0.0004	601 ± 4	2.98
D22B WHOI	1x	23.43 ± 0.53	12.50 ± 0.05	0.0338 ± 0.0005	3408 ± 79	2.93
D22B WHOI	1x	23.33 ± 0.51	11.49 ± 0.04	0.0317 ± 0.0003	1165 ± 30	2.85
D22B WHOI	1x	23.05 ± 0.58	12.50 ± 0.05	0.0331 ± 0.0005	3406 ± 70	2.87
D22B WHOI	1x	23.09 ± 0.57	10.98 ± 0.04	0.0312 ± 0.0004	916 ± 11	2.78
D22B WHOI	2x	22.25 ± 0.49	12.49 ± 0.05	0.0338 ± 0.0005	3021 ± 59	2.98
D22B WHOI	2x	23.06 ± 0.49	10.28 ± 0.04	0.0295 ± 0.0003	437 ± 3	2.84
D22B WHOI	3x	22.57 ± 0.53	9.97 ± 0.04	0.0289 ± 0.0003	348 ± 3	2.79
D22B WHOI	3x	22.85 ± 0.47	10.19 ± 0.04	0.0293 ± 0.0003	396 ± 2	2.91
D22B WHOI	3x	22.86 ± 0.38	12.13 ± 0.05	0.0327 ± 0.0004	2031 ± 22	2.81
D22B WHOI	3x	22.65 ± 0.37	10.01 ± 0.04	0.0289 ± 0.0003	349 ± 2	2.95
D22B WHOI	3x	23.53 ± 0.51	12.59 ± 0.05	0.0338 ± 0.0005	4722 ± 281	2.91
D22B WHOI	4x	23.07 ± 0.37	11.82 ± 0.05	0.0322 ± 0.0004	1517 ± 165	2.86
D22B WHOI	4x	23.05 ± 0.39	10.81 ± 0.04	0.0303 ± 0.0003	704 ± 9	2.93
D22B WHOI	4x	23.01 ± 0.40	10.72 ± 0.04	0.0306 ± 0.0004	636 ± 4	2.83
D22B WHOI	4x	22.92 ± 0.37	12.34 ± 0.05	0.0330 ± 0.0004	1362 ± 13	3.03
D22B WHOI	4x	22.68 ± 0.44	12.58 ± 0.05	0.0336 ± 0.0004	2706 ± 36	3.02
D22B WHOI	4x	23.03 ± 0.41	12.79 ± 0.05	0.0341 ± 0.0005	6147 ± 137	3.01
D22B WHOI	4x	22.84 ± 0.32	11.33 ± 0.04	0.0313 ± 0.0003	1095 ± 24	2.85
D22B WHOI	4x	23.33 ± 0.34	10.64 ± 0.04	0.0304 ± 0.0004	620 ± 4	2.88
D22B WHOI	5x	23.42 ± 0.40	11.91 ± 0.05	0.0328 ± 0.0005	1865 ± 93	2.83
D22B WHOI	5x	22.59 ± 0.54	12.16 ± 0.05	0.0331 ± 0.0004	2239 ± 42	2.99
D22B WHOI	6x	23.07 ± 0.34	12.85 ± 0.05	0.0332 ± 0.0004	6026 ± 127	2.97

Table 3: CO_2 and noble gas abundances of the pierced vesicles for the two Galápagos samples. Volumes of vesicles are calculated with the 3D Object Counter plugin of ImageJ. The CO_2 contents are calculated thanks to the pressure jump recorded on the manometer and calibrated with the air standard (refer to section 2.3). Errors are 1 sigma uncertainties. n.d. means not determined when gases from the vesicle are indistinguishable from the matrix blank.

Sample	Volume $x10^6$ µm^3	CO_2 $x10^{-4}$ cm^3	^{4}He $x10^{-9}$ cm^3	^{22}Ne $x10^{-13}$ cm^3	^{36}Ar $x10^{-13}$ cm^3
AHA-NEMO2-D22A vesicles					
V1	5.0	4.78 ± 0.23	6.72 ± 0.21	1.49 ± 0.18	2.45 ± 1.33
V2	18.2	15.6 ± 0.7	17.9 ± 0.5	3.97 ± 0.21	8.23 ± 1.35
V3	16.7	13.8 ± 0.6	18.8 ± 0.6	4.72 ± 0.23	11.5 ± 1.4
V4	16.9	15.8 ± 0.7	21.1 ± 0.6	4.18 ± 0.22	12.0 ± 1.4
AHA-NEMO2-D22B vesicles					
V1	4.0	3.27 ± 0.16	4.76 ± 0.15	1.29 ± 0.18	2.64 ± 1.33
V2	2.9	2.06 ± 0.12	3.19 ± 0.11	0.84 ± 0.18	1.77 ± 1.33
V3	2.4	1.83 ± 0.11	2.86 ± 0.10	1.11 ± 0.18	1.09 ± 1.33
V4	1.9	1.47 ± 0.11	1.73 ± 0.07	n.d.	2.23 ± 1.33
V5	10.7	7.82 ± 0.36	10.4 ± 0.3	1.99 ± 0.19	6.58 ± 1.35
V6	25.2	20.6 ± 0.9	27.6 ± 0.8	5.31 ± 0.24	13.2 ± 1.4

632 Table 4: Isotopic compositions of the pierced vesicles for the two Galápagos samples. Ra is the air
633 $^{3}He/^{4}He$ ratio equals to $1.384x10^{-6}$. $^{40}Ar^{*}$ is radiogenic ^{40}Ar. Errors are 1 sigma uncertainties. n.d. means
634 not determined when gases from the vesicle are indistinguishable from the matrix blank. We consider a
635 $^{40}Ar/^{36}Ar$ ratio of 298.6 for the air as obtained by Lee et al. (2006) to determine the $^{40}Ar/^{36}Ar$ and
636 $^{4}He/^{40}Ar^{*}$ ratios.

637

Sample	$CO_2/^{3}He$ $x10^{9}$	$^{3}He/^{4}He$ (x Ra)	$^{20}Ne/^{22}Ne$	$^{21}Ne/^{22}Ne$	$^{40}Ar/^{36}Ar$	$^{4}He/^{40}Ar^{*}$
AHA-NEMO2-D22A vesicles						
V1	2.28 ± 0.13	22.57 ± 0.25	12.09 ± 0.29	0.0326 ± 0.0023	9102 ± 2173	3.11 ± 1.86
V2	2.81 ± 0.16	22.42 ± 0.17	12.87 ± 0.20	0.0329 ± 0.0016	9407 ± 672	2.39 ± 0.44
V3	2.35 ± 0.13	22.54 ± 0.17	12.05 ± 0.15	0.0320 ± 0.0013	6260 ± 315	2.75 ± 0.37
V4	2.37 ± 0.13	22.87 ± 0.16	12.47 ± 0.16	0.0325 ± 0.0013	6306 ± 319	2.94 ± 0.38
AHA-NEMO2-D22B vesicles						
V1	2.16 ± 0.13	22.97 ± 0.33	11.43 ± 0.47	0.0295 ± 0.0031	6564 ± 1618	2.88 ± 1.64
V2	2.03 ± 0.14	22.97 ± 0.43	12.15 ± 0.71	0.0359 ± 0.0053	6310 ± 2536	3.01 ± 2.60
V3	2.06 ± 0.15	22.46 ± 0.48	11.08 ± 0.49	0.0333 ± 0.0035	8682 ± 5704	n.d.
V4	2.57 ± 0.23	24.01 ± 0.72	n.d.	n.d.	3283 ± 911	2.59 ± 1.74
V5	2.40 ± 0.13	22.63 ± 0.21	12.59 ± 0.42	0.0355 ± 0.0022	6061 ± 653	2.75 ± 0.65
V6	2.36 ± 0.13	22.89 ± 0.16	12.87 ± 0.25	0.0329 ± 0.0014	7408 ± 363	2.93 ± 0.35

638

639

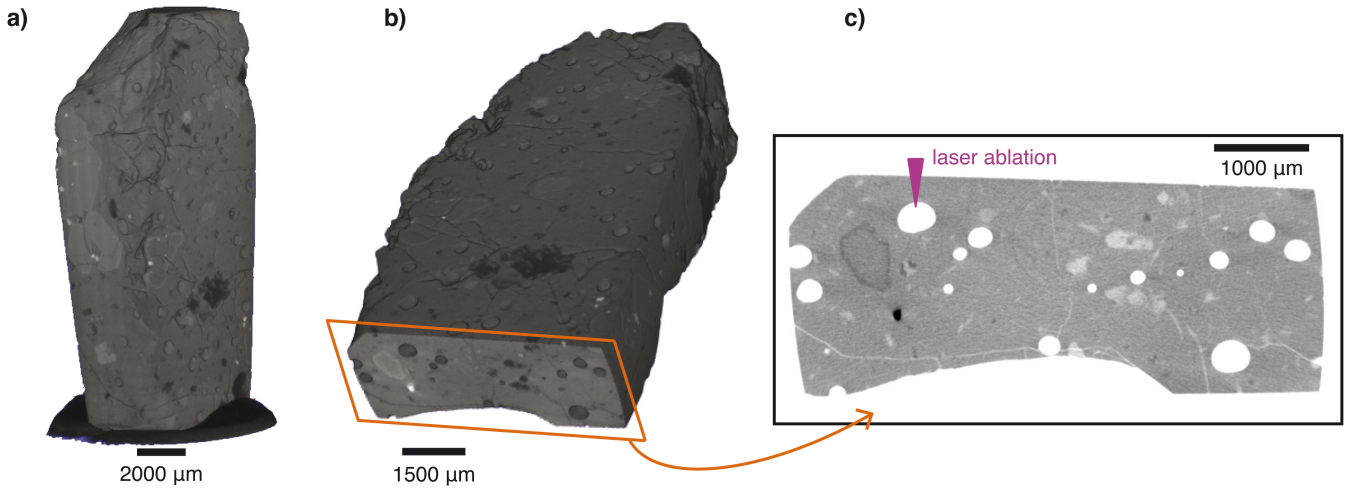

640

641

642 Figure 1: Principle for locating subsurface vesicles of sample AHA-NEMO2-D22B before laser ablation:
643 a 3D volume (a) is obtained from all the slices. A virtual cut through the object is shown in (b) and the
644 slice (c) represents one transverse section of the sample as shown in (b). On the slice (c), vesicles are in
645 white and the glass is in gray, as well as a few crystals. Some cracks are also visible and link some
646 vesicles to air (as the one in the lower right corner). On the slice (c) we can measure the vesicle depths
647 before piercing them with the laser.

648

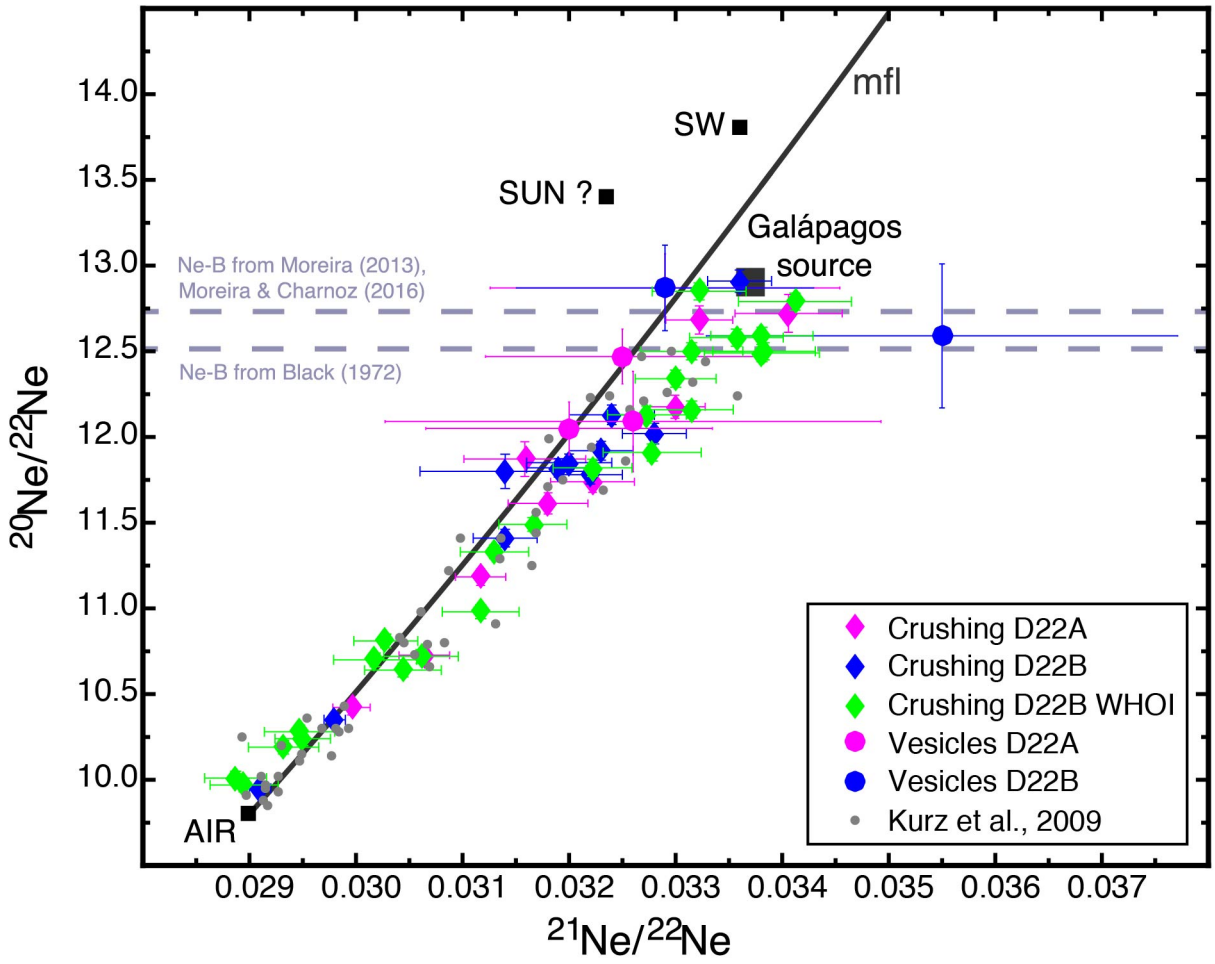

649

650 Figure 2: The three-neon isotope diagram, $^{20}Ne/^{22}Ne$ versus $^{21}Ne/^{22}Ne$, for analyses of step-crushing of
651 sample AHA-NEMO2-D22A (pink diamonds) and sample AHA-NEMO2-D22B (blue diamonds). Data
652 of single vesicles are also shown for sample AHA-NEMO2-D22A (mauve circles) and for the vesicles
653 V5 and V6 of sample AHA-NEMO2-D22B (blue circles). Only vesicles for which the matrix blank
654 contribution is less than 60 % are taking into account. (Refer to Table 2 and Table 4). For comparison,
655 individual step-heating and crushing results (for which ^{20}Ne is at least of $1x10^{-11}$ ccSTP) of Kurz et al.
656 (2009) for Fernandina samples are indicated in gray (small points) without their uncertainties in order
657 not to overload the figure. *mfl* stands for mass fractionation line and is obtained from a Rayleigh
658 distillation law (Sarda et al., 1988). SW: Solar wind (Heber et al., 2009), SUN (Heber et al., 2012), Ne-
659 B: Neon B, the value of 12.52 as defined by Black (1972) and the value of 12.73 proposed by Moreira
660 (2013) and Moreira and Charnoz (2016).

661

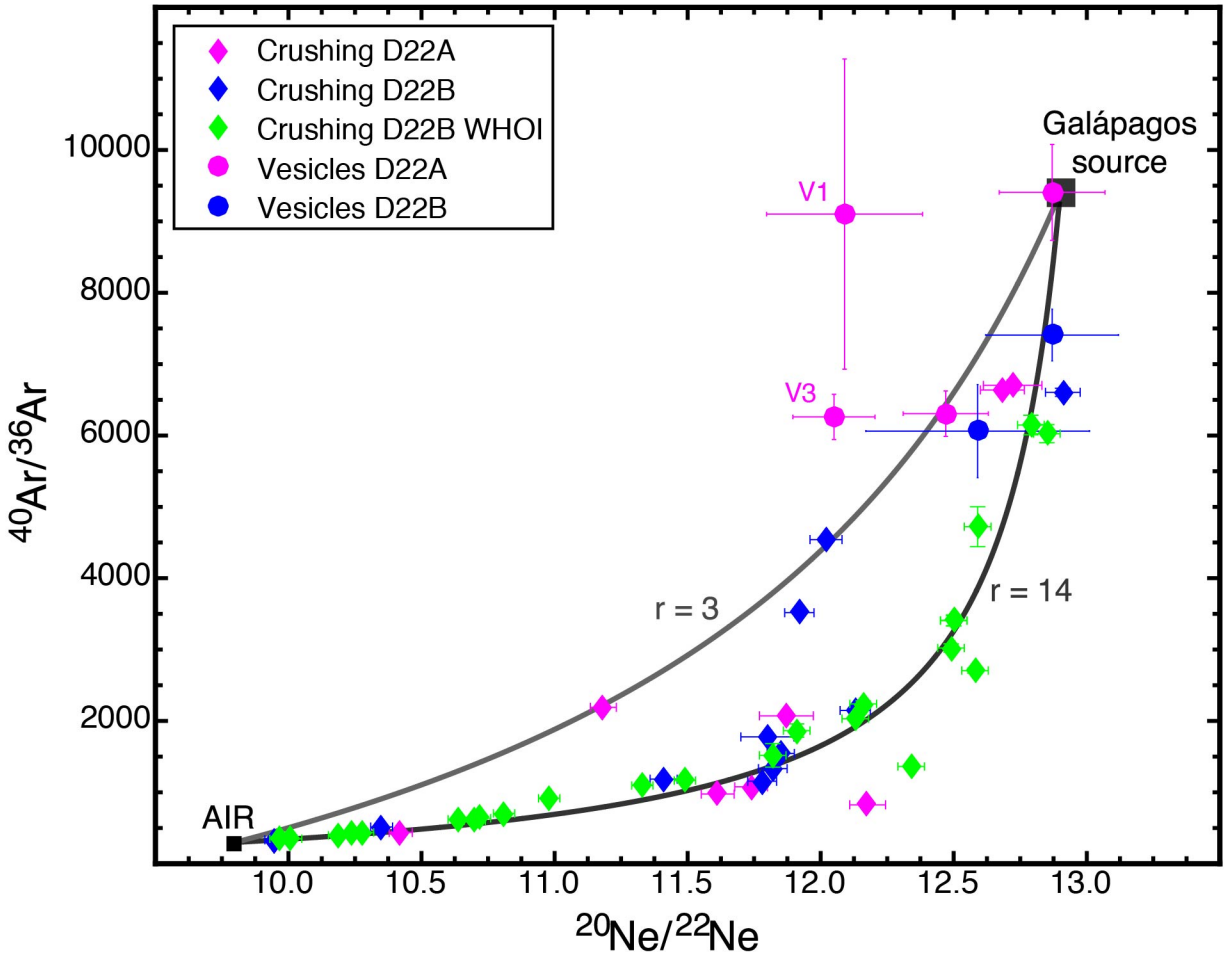

662

663

664 Figure 3: $^{40}Ar/^{36}Ar$ versus $^{20}Ne/^{22}Ne$ for the same data as in Figure 2, that is data of step-crushing for the
665 two Galápagos samples, data of single vesicles for sample AHA-NEMO2-D22A and data of the vesicles
666 V5 and V6 of sample AHA-NEMO2-D22B. Data of step-crushing show a mixture between an air-like
667 component and a mantle-like component. Two mixing hyperbolas have been drawn in order to fit the
668 data with r=3 and r=14. The *r* parameter indicates the hyperbola curvature and is equal to
669 $(^{36}Ar/^{22}Ne)_{AIR}/(^{36}Ar/^{22}Ne)_{MANTLE}$. The hyperbolas have been derived considering an air-like endmember
670 and a mantle endmember (with a $^{20}Ne/^{22}Ne$ ratio of 12.9 and a $^{40}Ar/^{36}Ar$ ratio of 9400).

671

672

673

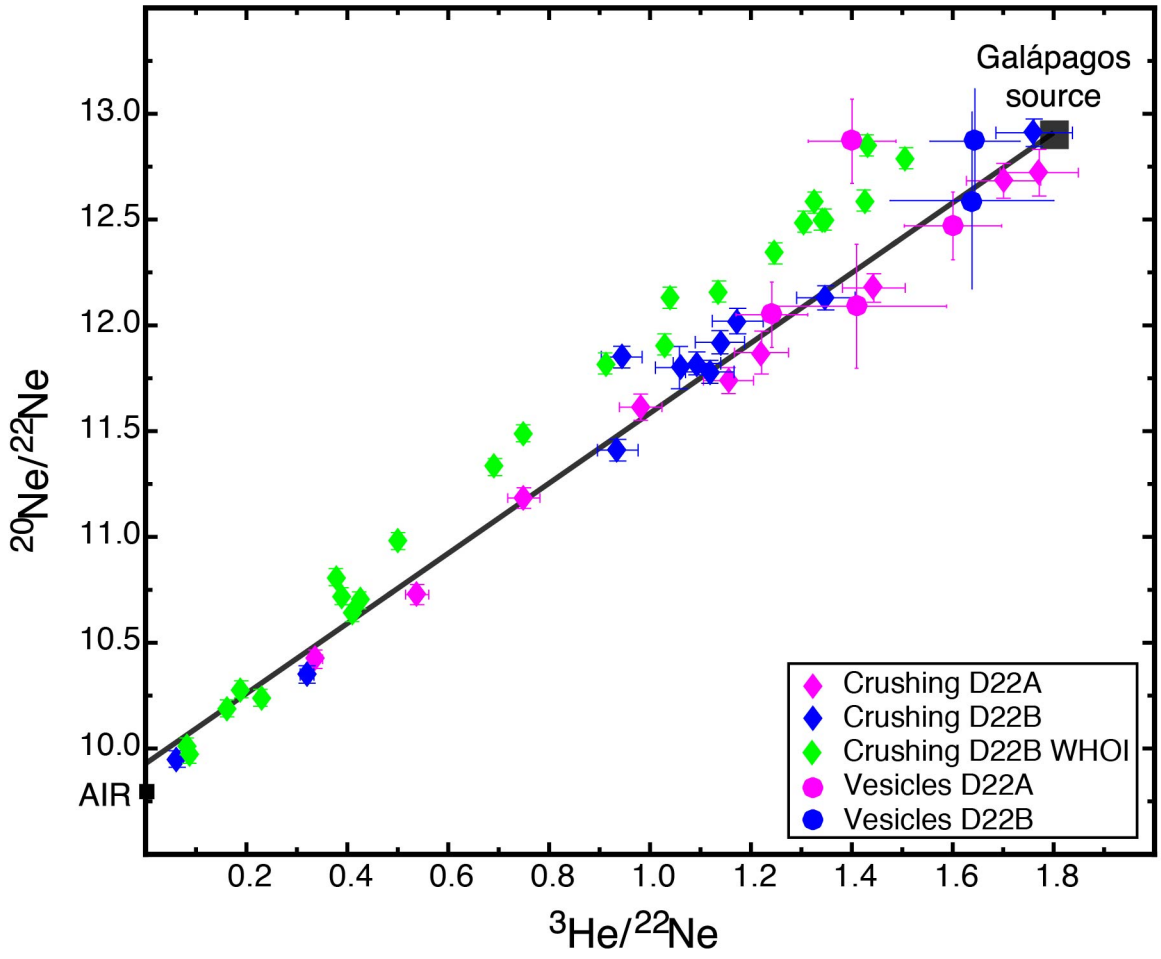

Figure 4: $^{20}Ne/^{22}Ne$ versus $^{3}He/^{22}Ne$ for the two Galápagos samples (same data as in Figure 2 that is data of step-crushing for the two Galápagos samples, data of single vesicles for sample AHA-NEMO2-D22A and data of the vesicles V5 and V6 of sample AHA-NEMO2-D22B). Data of step-crushing show a mixture between an air-like component and a mantle component.

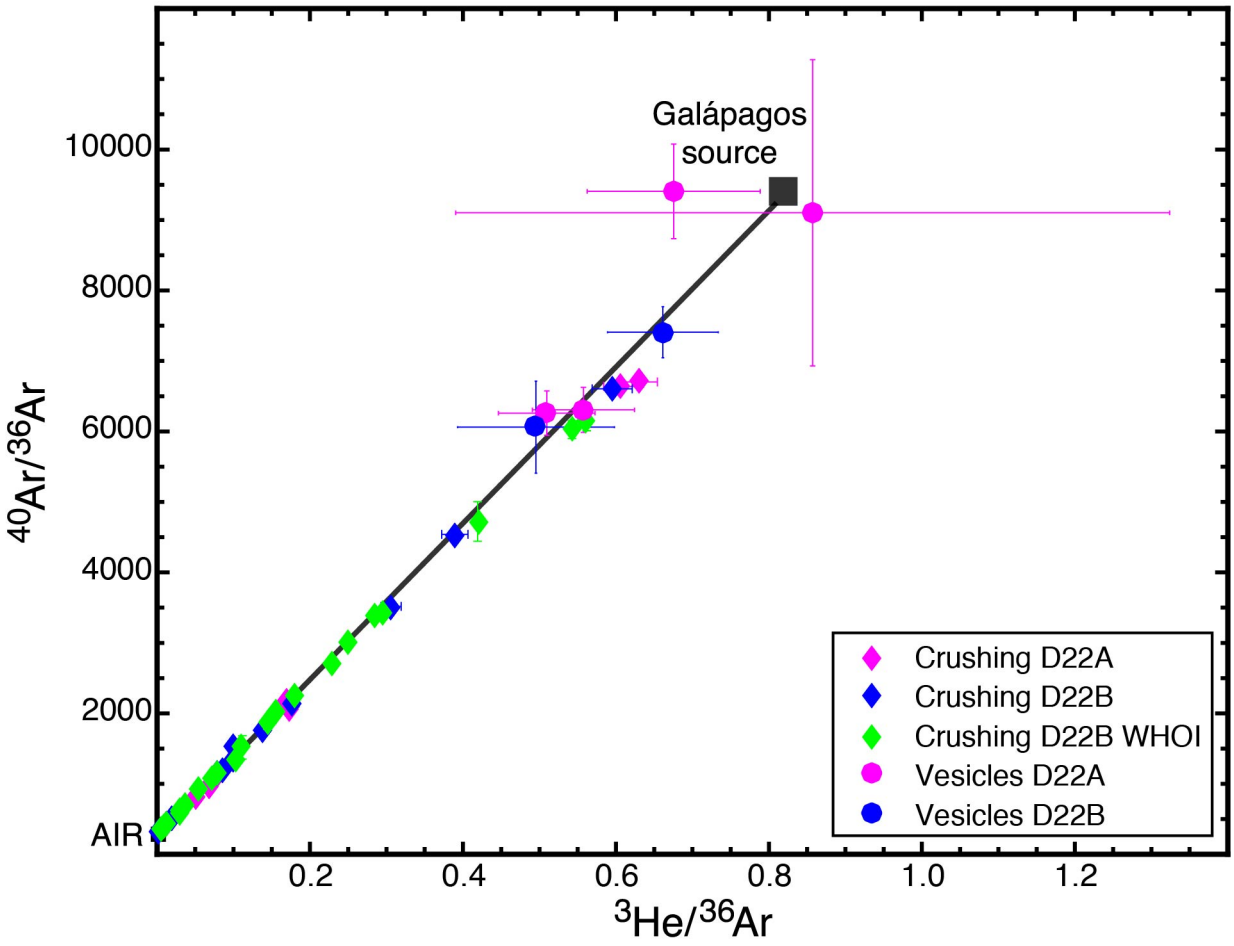

685

686 Figure 5: $^{40}Ar/^{36}Ar$ versus $^{3}He/^{36}Ar$ for the two Galápagos samples (same data as in Figure 2, that is data
687 of step-crushing for the two Galápagos samples, data of single vesicles for sample AHA-NEMO2-D22A
688 and data of the vesicles V5 and V6 of sample AHA-NEMO2-D22B). Data of step-crushing show a
689 mixture between an air-like component and a mantle component.

690

691

692